Article

Efficient perovskite solar cell on steel enabled by diffusion barrier and surface passivation

Jianghui Zheng, Fa-Jun Ma, Chwenhaw Liao, ..., David R. McKenzie, Shujuan Huang, Anita W.Y. Ho-Baillie

jianghui.zheng@sydney.edu.au (J.Z.)
anita.ho-baillie@sydney.edu.au (A.W.Y.H.-B.)

Highlights

17% efficient perovskite solar cell on steel is demonstrated

Indium tin oxide is an effective barrier against iron diffusion from steel

n-Octylammonium bromide surface treatment improves the cell performance on steel

Zheng et al. report a 17.1% efficient perovskite solar cell on steel, elucidating the important role of an indium tin oxide interlayer as a barrier against iron diffusion from the steel substrate. They also report an n-octylammonium bromide treatment surface to the perovskite, improving cell efficiency and stability.

Article

Efficient perovskite solar cell on steel enabled by diffusion barrier and surface passivation

Jianghui Zheng,[1,2,3,4,*] Fa-Jun Ma,[3] Chwenhaw Liao,[1,2] Jueming Bing,[1,2] Shi Tang,[1,2] Arman Mahboubi Soufiani,[3] Robert Lee Chin,[3] Chaowei Xue,[3] Jiangtao Qu,[5] Limei Yang,[5,6] Md Arafat Mahmud,[1,2] Zhenyu Sun,[3] Tik Lun Leung,[1,2] Guoliang Wang,[1,2] Julie M. Cairney,[5] Stephen Bremner,[3] David R. McKenzie,[1,2] Shujuan Huang,[3,4] and Anita W.Y. Ho-Baillie[1,2,3,7,*]

SUMMARY

While many state-of-the-art perovskite solar cells (PSCs) have been realized on rigid glass substrates, demonstrating perovskite cells on other types of surfaces may give rise to new applications. Here, we successfully demonstrate efficient PSCs on steel. The role of an indium tin oxide interlayer as a barrier against iron diffusion from the steel substrate is elucidated. We further show that the performance of the perovskite device on steel can be improved by using an n-octylammonium bromide passivation layer, achieving a power conversion efficiency of 17.1%. To the best of our knowledge, this is the highest reported for perovskite cells on steel. This work demonstrates the robust design necessary for PSCs on steel and the versatility of PSCs. It may also inspire work on other types of surfaces beyond glass, paving the way for a wider range of applications.

INTRODUCTION

The emergence of organic-inorganic hybrid perovskites has created a new field of photovoltaic research and development.[1] Remarkable progress has been made in perovskite solar cells' (PSCs') power conversion efficiencies (PCEs) from 3.8% to a certified 26.0% in 12 years.[2,3] State-of-the-art PSCs have usually been realized on a rigid glass substrate. For other applications such as design-integrated photovoltaics, perovskite cells can be fabricated on a lightweight flexible substrate followed by adhesive installation or direct fabrication of the cells onto the structure of interest. For the former, the lightweight substrates can be insulating, such as polyethylene terephthalate (PET),[4,5] polyethylene naphthalate (PEN),[6,7] and polyimide (PI),[8] or conducting, such as steel. Steel has good thermal stability, strength, and toughness as a substrate for PSC fabrication. However, it is opaque, thereby requiring a transparent electrode to complete cell fabrication. The advantage of being flexible and conductive means that the steel itself can act as both a substrate and an electrode for either large-area-monolithic-panel or smaller-area-singular single-junction[9,10] or multi-junction[9] cell fabrication.

In terms of PSCs on steel, in 2018, Feleki et al. reported an 11.4% efficiency perovskite cell on a coated steel substrate using a dielectric/metal/dielectric transparent top electrode.[11] In 2019, Kumar et al. reported a PSC on a flexible stainless substrate using a 200/100 nm SiO$_2$/Au stack as an interlayer between the steel and the

[1]School of Physics, The University of Sydney, Sydney, NSW 2006, Australia

[2]The University of Sydney Nano Institute (Sydney Nano), The University of Sydney, Sydney, NSW 2006, Australia

[3]Australian Centre for Advanced Photovoltaics, School of Photovoltaic and Renewable Energy Engineering, University of New South Wales, Sydney, NSW 2052, Australia

[4]Sustainable Energy Research Centre, School of Engineering, Macquarie University, Sydney, NSW 2109, Australia

[5]Australian Centre for Microscopy and Microanalysis (ACMM), The University of Sydney, Sydney, NSW 2006, Australia

[6]School of Civil & Environmental Engineering, University of Technology Sydney, 81 Broadway, Ultimo, NSW 2007, Australia

[7]Lead contact

*Correspondence:
jianghui.zheng@sydney.edu.au (J.Z.),
anita.ho-baillie@sydney.edu.au (A.W.Y.H.-B.)
https://doi.org/10.1016/j.xcrp.2023.101543

perovskite cell, achieving an efficiency of 3.45%.[12] In early 2022, Feleki et al. reported a 15.2% efficient n-i-p PSC on a Ni-plated high-gloss steel substrate using polyamide-imide (PAI) planarization coating to moderate the surface roughness of steel and by applying a Ti/indium tin oxide (ITO) layer as the electrode on the substrate side.[13] After this work, the same authors reported a 16.5% efficient PSC on steel using the similar steel-substrate preparation as before except the polarity in this instance was of p-i-n instead of n-i-p.[14]

In this work, we elucidate the role of an ITO interlayer for the demonstration of PSCs on steel substrates. In this work, a commercial roofing and paneling rigid steel material is used, but the learnings can also be applied on flexible steel material. We found that the device performance was significantly improved when an ITO interlayer was present between the prepared steel substrate and the PSC. Characterization and computer simulation showed that cells without an ITO interlayer suffer from low PCEs due to iron diffusion from the steel substrate into the PSC. A device with an 80 nm ITO interlayer achieved an efficiency of 15.3%, while the control device without an interlayer had an efficiency of 6.5%. Further surface passivation using n-octylammonium bromide (n-OABr) was found to enhance quality of the perovskite absorber, evidenced by enhanced photoluminescence intensity and carrier lifetime. When applied to cell demonstration on steel, a PCE of 17.1% was achieved, which is the highest for reported PSCs on steel to date (Table S1).

RESULTS AND DISCUSSION

Device structure

Figure 1 shows the schematic of a PSC on steel with a structure of steel/ITO/SnO$_2$/Cs$_{0.05}$FA$_{0.8}$MA$_{0.15}$Pb(I$_{0.85}$Br$_{0.15}$)$_3$/spiro-MeOTAD/MoO$_3$/ITO, whereby the SnO$_2$ is the electron transport layer, Cs$_{0.05}$FA$_{0.8}$MA$_{0.15}$Pb(I$_{0.85}$Br$_{0.15}$)$_3$ (FA = formamidinium and MA = methylammonium) is the photovoltaic absorber, spiro-MeOTAD is the hole transport layer, MoO$_3$ is the buffer layer, and the front or top ITO is the transparent electrode. Figure S1A shows the sequence of steel substrate preparation starting from the as-received substrate, to the prepared substrate, and lastly to fabricated cells on steel. Figure S1B shows the surface roughness or smoothness after substrate preparation for the side on which the cell will be fabricated, while the other side of the substrate remains intact. Figure 1B shows the cross-sectional scanning transmission electron microscopy (STEM) image of the device with an ITO interlayer showing good coverage of the steel substrate. Figure 1C shows the energy-dispersive spectroscopy (EDS) maps of the device with an ITO interlayer showing uniform distributions of the key elements. Key elements in each layer can be clearly seen, e.g., indium and oxygen in the top ITO, molybdenum in the MoO$_3$ layer, lead (Pb) in the perovskite layer, and carbon in the spiro-MeOTAD layer. The Pt layer that serves to eliminate charge buildup for STEM can also be seen. It is important to note that the presence of iron at the steel surface will become important for device performance as discussed in the later sections.

Effect of ITO interlayer

Figure 2 shows the distribution of electrical characteristics for 10 perovskite devices on steel without and with an 80-nm-thick ITO interlayer, as a thinner ITO interlayer resulted in poorer device performance (Figure S2). The performance of devices with the ITO interlayer more than doubled compared with those without the ITO interlayer. The former produced higher average values of open-circuit voltage (V_{OC}) (1,072 mV), short-circuit current density (J_{SC}) (18.3 mA/cm^2), fill factor (FF) (0.67), and PCE (13.2%), while the latter produced average values of
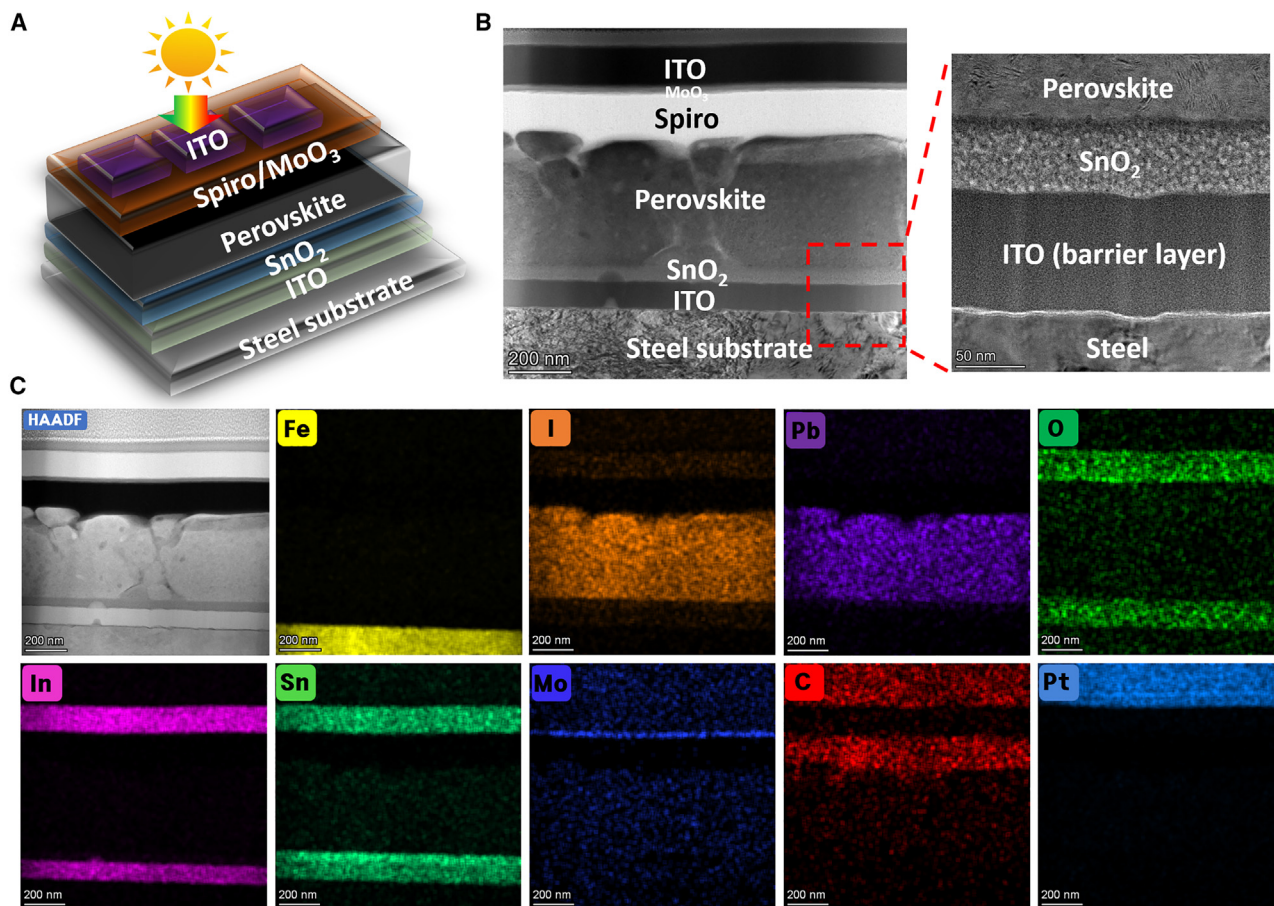
Figure 1. Schematic illustration and cross-sectional images of PSCs on steel

(A and B) Schematic (A) and cross-sectional scanning transmission electron microscopy (STEM) image (B) of the perovskite solar cell on steel with an ITO interlayer: steel/ITO/SnO$_2$/perovskite/spiro-MeOTAD/MoO$_3$/ITO.

(C) Bright-field cross-sectional image of the structure and its corresponding energy-dispersive spectroscopy (EDS) maps showing elements Fe, I, Pb, O, In, Sn, Mo, C, and Pt.

V_{OC} = 763 mV, J_{SC} = 17.2 mA/cm^2, FF = 0.46, and PCE = 6%. The benefit of ITO inclusion is shown in the steady-state photoluminescence (PL) images and the time-resolved PL (TRPL) traces of the perovskite layer as shown in Figures S3A–S3D. Both PL intensity and carrier effective lifetime of the perovskite layer deduced from the TRPL increased, from 360 to 443 ns, after the inclusion of the ITO interlayer. Figure 2E show the current density-voltage (J-V) curves and the photovoltaic parameters of the champion devices with and without the ITO interlayer. Figure 2F shows the steady-state efficiency (15.1%) of the champion device with the ITO interlayer due to the improvements in both the V_{OC} by 336 mV and the FF by 24% (absolute).

To clarify the beneficial role of the ITO interlayer, we first examined the surface topology of the SnO$_2$ and perovskite film on the steel substrate with and without the ITO interlayer using conductive atomic force microscopy (c-AFM), and the results are shown in Figure S4. It was observed that the SnO$_2$-coated steel substrate with the ITO interlayer has a lower root-mean-square (RMS) value of surface roughness. This may explain the larger grain size observed for the perovskite film deposited on such a surface compared with that without the ITO interlayer. The resultant
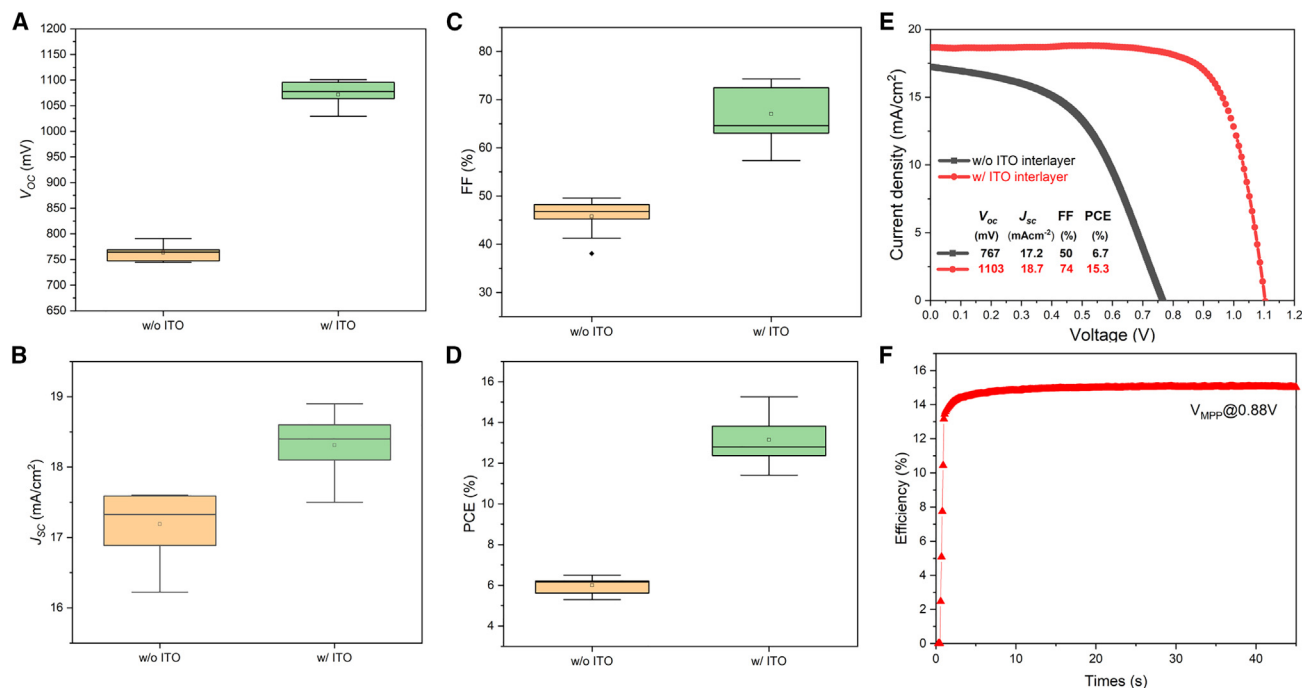
Figure 2. Photovoltaic performance of PSCs on steel with and without the ITO interlayer

(A–D) Distribution of (A) open-circuit voltage (V_{OC}), (B) short-circuit current density (J_{SC}), (C) fill factor (*FF*) (D), and power conversion efficiency (*PCE*) for 10 PSCs on steel with and without the (80 nm) ITO interlayer. The upper "whisker" is the maximum measured. The upper bar of the box is the 75th percentile value. The middle bar is the median value. The square mark is for the average. The lowest bar is the 25th percentile value. The lower "whisker" is the minimum value.

(E) Current density-voltage (*J-V*) curves of the champion devices with and without ITO.

(F) Steady-state efficiency of the champion device with ITO.

better-quality perovskite film may be one of the contributors to the higher current observed in corresponding devices than seen in those without (Figure 2B).

Other possible mechanisms are therefore investigated to explain the poorer performance of ITO-interlayer-free cells. It is known that ITO can act as a diffusion barrier,[15,16] and in this case, iron from the steel substrate. We therefore verify this via time-of-flight secondary ion mass spectrometry (TOF-SIMS). Results in Figure 3A show severe iron diffusion right through the SnO_2 into the perovskite absorber in the absence of the ITO barrier layer, while iron diffusion is limited into the ITO interlayer only, as shown in Figure 3B.

To investigate the effect of Fe diffusion into the SnO_2 layer, we conducted ultraviolet photoelectron spectroscopy (UPS) (Figure S5). Results show the increase in SnO_2 work function from 4.61 ($\Phi_{(ITO-present)}$) to 4.97 eV ($\Phi_{(ITO-free)}$) if the ITO interlayer was removed (Figure S5). Others have reported that p-type SnO_2 thin film is achievable by Fe doping.[17] The energy band diagram of the device with or without the ITO layer is shown in Figure S6.

In terms of the effect of iron diffusion on the perovskite absorber, Poindexter et al. have reported that iron contamination in lead halide PSCs results in significant V_{OC} and J_{SC} drops when the iron concentration exceeds 10 ppm due to the increase in deep-level defects.[18] A voltage drop more than 300 mV was observed with 100 ppm of iron contamination, which is similar to what is observed in our work,
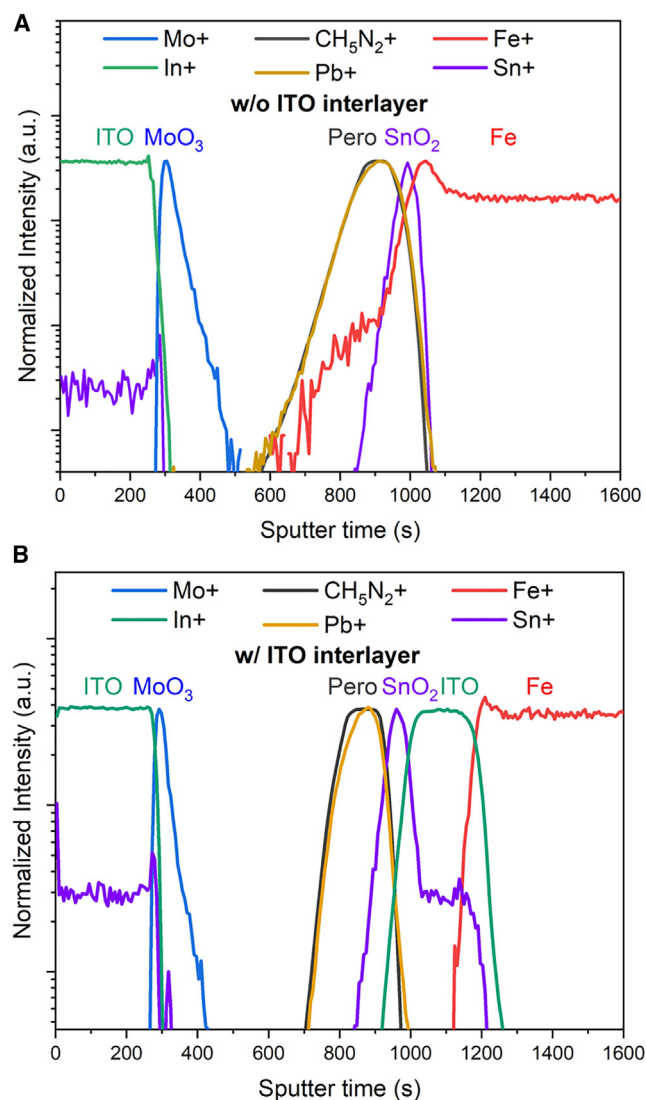
Figure 3. Time-of-flight secondary ion mass spectrometry (TOF-SIMS) analysis
TOF-SIMS of perovskite on the steel substrate (A) without and (B) with an ITO interlayer.

although our carrier lifetime might have been over-estimated (363 ns in our case compared with 138 ns reported by Poindexter et al.).

To simulate such effect on *J-V* curves, we first modeled the champion cell with the ITO using the parameters listed in Table S2. A trap-assisted tunneling mechanism was assumed for MoO_3 to effectively collect holes from the spiro-MeOTAD layer to the ITO top electrode. Figure S7A shows the good agreement between simulated and experimental *J-V* curves for the ITO-containing cell. For the ITO-interlayer-free cell, Figure S7B shows the effect of increasing the SnO_2 work function. FF deteriorates with an increasing SnO_2 work function that decreases the built-in potential, making electron extraction difficult. This results in an "S-shaped" *J-V* curve with a lower FF once the SnO_2 work function exceeds 4.66 eV, which is what is observed in our ITO-interlayer-free cells. A better fit to the experiential *J-V* curve will be achieved using a realistic series resistance (R_S) value and a reduced carrier lifetime, although our experimentally determined carrier lifetime of 360 ns is still too high and
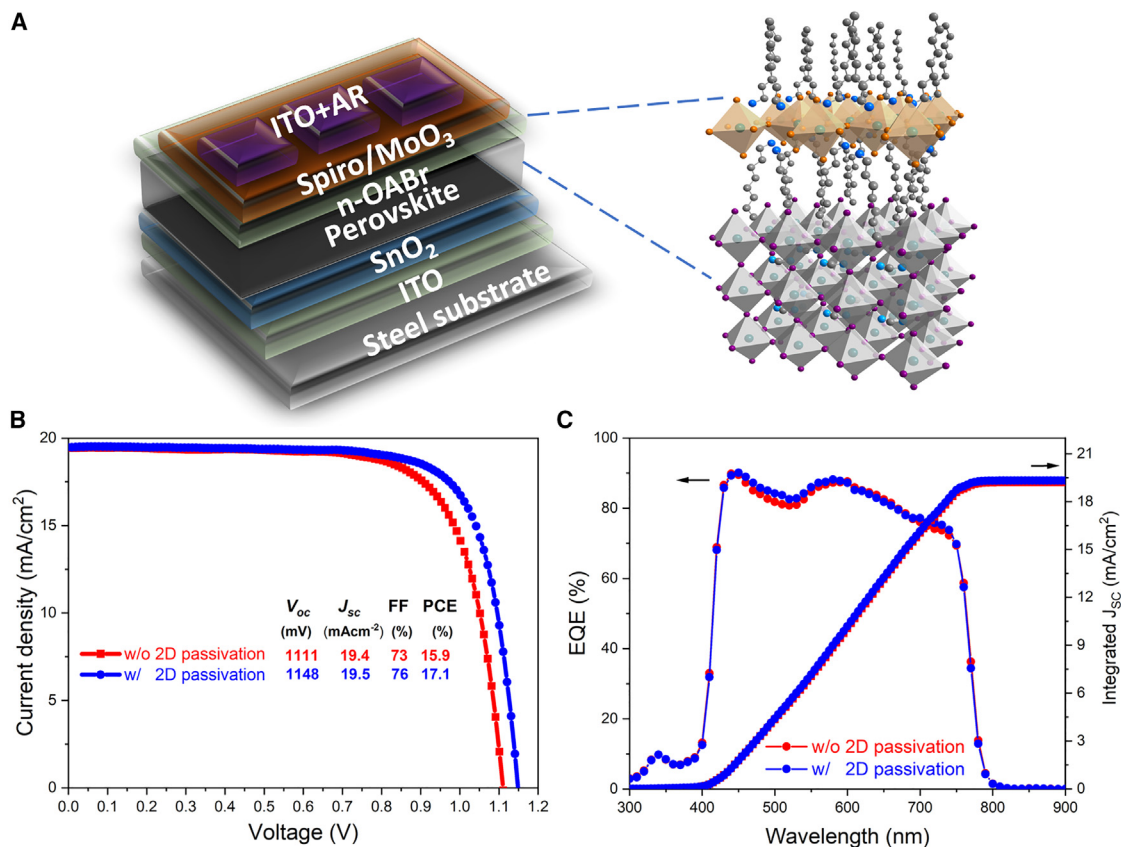
**Figure 4. Photovoltaic performance of PSCs on steel with and without n-OABr**

(A) Schematic of the n-octylammonium bromide (n-OABr)-passivated perovskite solar cell on steel with ITO interlayer: steel/ITO/SnO$_2$/perovskite/passivation layer/spiro-MeOTAD/MoO$_3$/ITO/antireflection layer.

(B and C) J-V curves (B) and external quantum efficiency (EQE) curves (C) of the champion devices with and without passivation.

would only cause a voltage drop of around 7 mV. Further investigation will be required to investigate all possible causes for significant V_{OC} drops (>330 mV) in ITO-interlayer-free devices.

Effect of surface passivation layer

To further improve the performance of perovskite cells on steel, we applied the passivation strategy using a bromide-containing long alkyl chain organic cation n-OABr, which also has been demonstrated to be effective in passivating 1.72 eV high-band-gap perovskites (FA$_{0.75}$MA$_{0.15}$Cs$_{0.1}$Rb$_{0.05}$PbI$_2$Br).[19] Figure 4A shows the schematic of the passivated device demonstrated. From here on, ITO interlayers were included in all samples unless specified otherwise. To characterize the passivated perovskite film, X-ray diffraction (XRD) measurements were performed, and the results are shown in Figure S8 for non-passivated (red) and passivated (n-OABr) perovskites (blue) deposited on the SnO$_2$/ITO substrate, which is steel or glass for comparison. Passivated perovskite film shows the presence of an additional low angle peak at around 10.3° under both XRD and grazing-incidence XRD (GIXRD) confirming the formation of a 2D perovskite. Interestingly, when a steel substrate is used, the 2D perovskite peak intensity is stronger (Figure S8D) and the PbI$_2$ peak intensity is weaker (Figure S8E) compared to glass. Further work will be carried out to understand how steel substrates better aid in the formation of 2D perovskite surface layers with fewer PbI$_2$ residuals on a 3D perovskite bulk film than glass substrates. Fewer
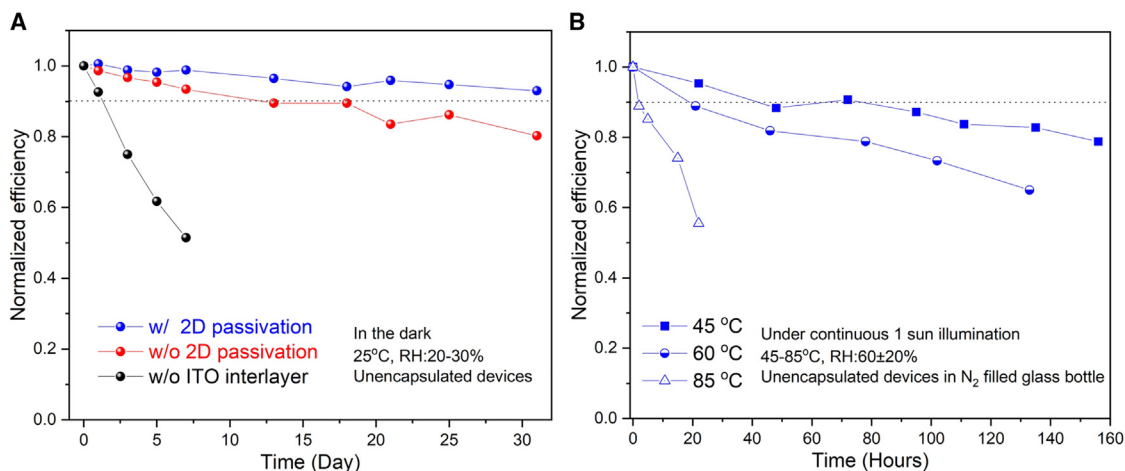
Figure 5. Stability of un-encapsulated cells
(A) During 31 day storage in the dark at 25°C and 10%–20% relative humidity (RH).
(B) Each in sealed, N_2-filled glass bottle under continuous 1-sun illumination at temperature 45°C, 60°C, or 85°C.

PbI_2 residuals were also observed after passivation (cf. Figures S9A and S9B) under both XRD and SEM. There is no significant change on perovskite grain size after passivation.

The existence of nOA ions in the passivated perovskite film was also confirmed by the results of Fourier transform infrared (FTIR) measurements (Figures S9C and S9D) via the presence of additional peaks at 2,855 and 2,926 cm^{-1}, which are the asymmetric vibrations of the C–C group in long alkyl chain organic cations.

The positive impact of passivation can be seen in the results of steady-state PL and TRPL showing enhanced PL intensity (Figure S10A) and carrier lifetime (Figure S10B). This in turn contributes to improved voltage output and FF of passivated cells. The champion device produced an enhanced efficiency of 17.1% (Figure 4B)—which is the highest to date for perovskite cells on steel (Table S1). It can be seen that the improvement in current output for passivated cells is almost negligible (Figures 4B and 4C). In fact, J_{SC} of these devices is still below 20 mA/cm^2 even after the use of an antireflection (AR) layer. This is due to the high parasitic light absorption in the sun-facing 2,2′,7,7′-Tetrakis[N,N-di(4-methoxyphenyl)amino]-9,9′-spirobifluorene (spiro-OMeTAD)/MoO$_3$ stack contributing to current output losses, especially in the short wavelength region.[20,21] To overcome this problem, NiO$_x$[20,22] with better refractive index matching or a thinner spiro-OMeTAD-like material such as spiro-TTB[23] or p-i-n perovskite cell[14,24] can be used to further reduce the parasitic light absorption.

Device stability
Finally, we observed better stability of passivated (un-encapsulated) devices with an ITO interlayer stored for 31 days in the dark at 25°C and 20%–30% relative humidity compared with control devices (those without passivation, and those with no passivation nor ITO interlayer) as shown in Figure 5. The poorer stability of the ITO-free device is likely to be due to the presence of iron in the perovskite to sustain stable operation. Improved stability after passivation is due to the more hydrophobic surface[25] as observed from the results of contacting angle measurement (Figure S11). To evaluate device thermal and light stability, we illuminated the devices (with ITO interlayer and passivation) continuously at 1 sun at

45°C, 60°C, or 85°C. Results are shown in Figure 5B. While a device maintained 79% of its initial performance after 156 h of continuous illumination at 45°C, devices experienced a more rapid performance drop with increasing temperature. This is mainly due to the poor thermal stability of spiro-MeOTAD and the dopants.[26–29] Device instability at an elevated temperature may also be due to possible iron diffusion to the perovskite even in the presence of an ITO interlayer as shown via depth-resolved X-ray photoelectron spectroscopy (XPS) of a device after 132 h of illumination at 60°C (Figure S12). Further work will be required to further optimize the interlayer design to improve robustness against metal diffusion. This includes the exploration of materials alternative to ITO such as SiO_2,[30] TiN,[31] and Ti,[32] which have been reported to be effective Fe diffusion barriers.

In summary, an efficient PSC on steel has been demonstrated. It found that the ITO interlayer between the perovskite cell and the steel substrate is an effective barrier against iron diffusion from the steel substrate into the SnO_2 layer and the perovskite absorber, which increases the SnO_2 work function and affects the quality of perovskite absorber. The presence of the ITO interlayer also allows the formation of an ohmic contact between the SnO_2 layer and the steel substrate. All of these factors contribute to improved performance for cells to over 15% efficiency with an 80 nm ITO interlayer. Furthermore, the efficiency and stability of the perovskite device on steel were further improved via n-OABr surface passivation, producing a champion PCE of 17.1%. This is the highest value to date for perovskite cells on steel. This work inspires future work where different materials as an interlayer could be investigated and where cells using materials with better refractive index matching can be demonstrated with the aim of further boosting the performance and stability of perovskite cells on steel.

EXPERIMENTAL PROCEDURES

Resource availability

Lead contact
Further information should be directed to the lead contact, Anita W.Y. Ho-Baillie (anita.ho-baillie@sydney.edu.au).

Materials availability
This study did not generate new unique materials.

Data and code availability
The published article and its supplemental information include all data generated or analyzed during this study.

Fabrication of devices
COLORBOND steel was used because of its popularity for roofing and paneling and its availability. One side of the steel was first polished by 300 mesh sandpaper to remove surface paint and coating. The polishing was then refined using 1,000 mesh sandpaper, then 2,000, 3,000, and 4,000 mesh sandpaper to achieve a smooth surface. Polishing liquid (MasterPrep, Suspension Al_2O_3, 0.05 μm) was used for the final polishing process. Polished steel substrates were then cleaned by sonication in de-ionized water with 2% Hellmanex, de-ionized water, acetone, and isopropanol for 15 min in each step. For cells containing an interlayer, ITOs of different thicknesses (40, 80, or 120 nm) were deposited onto the substrates by sputtering with an radio frequency (RF) power of 30 W and Ar at 1.5 mTorr using an AJA International sputtering system. For SnO_2 deposition, substrates were first treated using an ultraviolet-ozone (UVO) cleaner for 5 min. SnO_2 colloidal nanoparticle solution (tin(IV) oxide,

15% in H_2O colloidal dispersion, Alfa Aesar) was diluted with H_2O to 3.75%, which was then spin coated onto the front of the substrate at 2,000 rpm for 30 s, followed by baking on a hotplate at 150°C for 10 min in air to form a 15–20 nm compact SnO_2 electron transport layer. A $Cs_{0.05}FA_{0.8}MA_{0.15}Pb(I_{0.85}Br_{0.15})_3$ (where FA = $HC(NH_2)_2$ and MA = CH_3NH_3) precursor was then spin coated onto the substrate at 2,000 rpm for 20 s, followed by 6,000 rpm for 30 s. During the spin coating, chlorobenzene (Sigma-Aldrich) was quickly dispensed 5 s before the end of the spin process. The perovskite film was then annealed at 100°C for 10 min, producing a dark brown dense color. For the deposition of hole transport material (HTM), the spiro-OMeTAD (Lumtec) precursor was first prepared by dissolving 72.3 mg spiro-OMeTAD, 28.8 μL 4-*tert*-butylpyridine (Sigma-Aldrich), 17.4 μL lithium bis(trifluoromethylsulphonyl)imide (Sigma-Aldrich) solution (520 mg/mL in acetonitrile, Sigma-Aldrich), and 29 μL FK209-cobalt(III)-TFSI (Lumtec) solution (300 mg FK209-cobalt(III)-TFSI in 1 mL acetonitrile) in 1 mL chlorobenzene (Sigma-Aldrich). The spiro-OMeTAD precursor was then deposited onto the perovskite layer by spin coating at 3,500 rpm for 30 s. Next, 15 nm MoO_3 (Sigma-Aldrich) was deposited onto the spiro-OMeTAD by thermal evaporation under vacuum at 5×10^{-5} mTorr. To complete cell fabrication, a transparent electrode was then fabricated by sputtering 130 nm ITO through a metal mask (defining device area of 0.09 cm^2) onto the MoO_3 layer with a 30 W RF power and Ar at 1.5 mTorr using the AJA International sputtering system. Rear sides of the steel substrates were left intact.

Characterizations

J-V measurements of the solar cells were performed using a solar cell current-voltage (*I-V*) testing system from ABET Technologies (using class AAA solar simulator) under an illumination power of 100 mW cm^{-2} with metal aperture (0.09 cm^2) and a scan rate of 30 mV s^{-1} from the V_{OC} to the J_{SC} direction (1.15 to −0.1 V). Probing was done by direct contact with the ITO front electrode (with care, e.g., minimum pressure) and by direct contact with the bulk steel substrate.

For cross-sectional imaging of the perovskite on steel samples, an FEI Themis Z double-corrected STEM equipped with Super X 4 silicon drift detectors (large collection angle of 0.9 srad) was used for TEM imaging. The high-angle annular dark-field imaging (HAADF) image was collected at a 115 mm camera length at a screen current of 50 pA. The EDS data were collected at a 0.1 nA current. The TEM foil was prepared by a Thermo Fisher Helios G4 Plasma Focused Ion Beam (PFIB) dual-beam platform following a standard lift-out protocol.[33] The samples were initially deposited with a 1-μm-thick Pt protective layer on the surface and then were cut into a 2 × 10 μm cantilever in the PFIB with 30 kV/15 nA voltage/current ion beam setting. After that, the samples were transferred to a half Cu TEM grid by a tungsten micromanipulator, followed by a few steps of foil thinning-down processes by reducing the current. The specimen was ready for TEM imaging after final polishing with 5 kV and 30 pA voltage/current beam setting. Finally, FEI Velox 3.3.1 and Gatan GMS 3.5 were used for the TEM data analysis.

The 3D optical image of the steel surface was measured using a TopMap Micro.View+ system.

c-AFM on perovskite and SnO_2 layers on the steel substrate were conducted out using a Bruker dimension icon SPM (USA) with a SCM-PIT-V2 probe via PeakForce TUNA mode. The samples were scanned at rate of 0.70 Hz and a resolution of 300 samples per line. Gwyddion 2.62 software was used to process the c-AFM data.

PL imaging measurements on perovskite layers on steel were performed at circa 1-sun equiv photogenerated flux using an in-house-constructed measurement setup. The illumination source was composed of arrays of light-emitting diodes (LEDs) with peak wavelengths of 630 nm. The calibration of the light-source intensity, after passing through the short-pass filtering, was performed using a poly-silicon solar cell (area: 4 cm^2) with a known photogenerated current at 1-sun illumination intensity. Images were collected using an sCMOS camera, immediately after the photoexcitation of the device, with short exposure times of $\leq$50 ms. A 685 nm long-pass filter with OD-7 in the blocking wavelength range was used in front of the camera lens at the detection side to prevent reflected and scattered excitation from reaching the camera detector.

TRPL measurements on perovskite layers on steel were performed using a customized micro-PL microscope. The excitation source was a 532 nm laser with pulse full-width at half-maximum of 10 ps and repetition rate of 1/6 MHz. This was focused onto the sample with a 50×/0.6 NA refractive objective, giving an average spot size estimated at 1,000 μm and an average power of 10 mW. The initial excess charge carriers were estimated to be on the order of 10^{16} cm^{-3}. The PL emitted from the excitation side was coupled back though the objective (epi-illumination), and the reflected 532 nm excitation was filtered using a 600 nm long-pass filter before detection by a fiber-coupled avalanche photodiode (ID110, instrument response time of $\sim$200 ps). The TRPL decay was interpreted using a single-photon counting card (Timeharp260) with time bins of 200 ps.

To determine the effective carrier lifetime (τ_{eff}), TRPL traces were converted into the injection-dependent carrier lifetime using the relationship between the PL intensity and the excess carrier density (Δn) at high injection levels, PL $\propto \Delta n$,[2] and the carrier continuity equation under transient excitation: $d(\Delta n)/dt = -dn/\tau_{eff}$. We first converted the TRPL intensity into Δn using the initial excess carrier density injected by the ultrafast laser pulse (full-width at half-maximum of <10 ps):

$$\Delta n(t = 0) = Abs \times P_{avg} / \left(A_{spot} \times f_{laser} \times E_{photon} \right).$$

Here, Abs is the sample absorptivity at the laser excitation wavelength, P_{avg} is the average laser power on the sample, f_{laser} is the laser repetition rate (1 MHz), E_{photon} is the photon energy, and A_{spot} is the excitation spot area assuming that $A_{spot} = \pi/4 \times D_{spot}^2$, where D_{spot} is the full-width at half-maximum spot size. We then calculated τ_{eff} from the Δn decay as $\tau_{eff}(\Delta n) = \Delta n/(-d(\Delta n)/dt)$.

TOF-SIMS was performed by ION-TOF TOFSIMS 5 equipment in positive polarity (Bi^{3+} at 30 keV, sputtered by Cs+ beam of 1 keV) in MCs+ mode.

XRD patterns were measured using a Bruker ECO D8 diffractometer with a Cu-Kα (λ = 1.5418 Å) radiation. GIXRD patterns were measured using PANalytical Empyrean thin-film X-ray diffractometer with Cu-Kα radiation with incident angle fixed at 2°.

FTIR spectra were performed using a Bruker Alpha portable spectrometer using the Platinum attenuated total reflectance single-reflection module.

To determine the work function (Φ) of the SnO$_2$ layer, UPS was performed using an ESCALAB250Xi, Thermo Scientific (UK). The Φ was calculated according to the formula Φ = hν (21.22 eV) – Ecutoff-measured.

Canon EOS200D with Laowa microlens 60 mm F2.8 was used to carry out the contact angle measurements.

For thermal and light stability testing, unencapsulated devices were placed in a sealed, N_2-filled glass bottle and then placed inside a Xe environment chamber for continuous illumination (100 mW/cm^2). The xenon lamp is from QUALITEST. The ambient relative humidity was at 60% $\pm$ 20% and the chamber temperature was set to 45°C, 60°C, or 85°C during the measurement. The devices were taken out of the Xe environment chamber and glass bottle for *J-V* measurement in the ambient atmosphere for $\approx$ 5–10 min each time and placed back into the chamber.

Depth-resolved XPS is measured using a Themo Fisher Scientific ESCALab 250 using a monochromate Al-Kα X-ray source (=1,486.68 eV) under high vacuum. The etching was achieved by an Ar cluster ion beam.

All measurements were undertaken at room temperature in ambient conditions.

Simulations
For modeling the device operation of the solar cells, a commercial software package, Sentaurus technology computer-aided design (TCAD),[34] was used. Photogeneration within each layer was computed with the simple optical beam absorption method using the Beer-Lambert law. The complex refractive index of each layer was obtained from in-house characterization. The key semiconductor material parameters for electrical simulation are listed in Table S1 and were obtained either from in-house characterization or from the literature as shown in the supplemental information. The ambient temperature in the simulation was set at 298.15 K to match the standard testing condition.

AUTHOR CONTRIBUTIONS
J.Z and F.-J.M. contributed equally to this work. J.Z. and A.W.Y.H.-B. conceived and designed all the experimental work. J.Z. carried out device fabrications and

conducted most characterizations. F.-J.M carried out device simulations. A.M.S. and R.L.C performed the PL-based measurements and analyses. C.X. provided advice on steel polishing. J.Q. and L.Y., supervised by J.M.C., performed STEM measurements and analysis. C.L. performed XRD and depth-resolved XPS measurements. S.T. performed c-AFM measurements, and T.L.L. analyzed the results. Z.S performed GIXRD measurements. The manuscript was written by J.Z. and A.W.Y.H.-B. All authors contributed to the discussion of the data, writing of the sections of the manuscript, and revision of the manuscript. The overall project was supervised by A.W.Y.H.-B.

DECLARATION OF INTERESTS

A.W.Y.H.-B. is an advisory board member at *Cell Reports Physical Science.*

REFERENCES

1. Green, M.A., Ho-Baillie, A., and Snaith, H.J. (2014). The emergence of perovskite solar cells. Nat. Photonics *8*, 506–514. https://doi.org/10.1038/nphoton.2014.134.

2. Green, M.A., and Ho-Baillie, A. (2017). Perovskite Solar Cells: The Birth of a New Era in Photovoltaics. ACS Energy Lett. *2*, 822–830. https://doi.org/10.1021/acsenergylett.7b00137.

3. NREL. https://www.nrel.gov/pv/cell-efficiency.html (Accessed 23th June 2023).

4. Qiu, W., Paetzold, U.W., Gehlhaar, R., Smirnov, V., Boyen, H.-G., Tait, J.G., Conings, B., Zhang, W., Nielsen, C.B., McCulloch, I., et al. (2015). An electron beam evaporated TiO$_2$ layer for high efficiency planar perovskite solar cells on flexible polyethylene terephthalate substrates. J. Mater. Chem. *3*, 22824–22829. https://doi.org/10.1039/C5TA07515G.

5. Ye, F., Tang, W., Xie, F., Yin, M., He, J., Wang, Y., Chen, H., Qiang, Y., Yang, X., and Han, L. (2017). Low-Temperature Soft-Cover Deposition of Uniform Large-Scale Perovskite Films for High-Performance Solar Cells. Adv. Mater. *29*, 1701440. https://doi.org/10.1002/adma.201701440.

6. Yoon, H., Kang, S.M., Lee, J.-K., and Choi, M. (2016). Hysteresis-free low-temperature-processed planar perovskite solar cells with 19.1% efficiency. Energy Environ. Sci. *9*, 2262–2266. https://doi.org/10.1039/c6ee01037g.

7. Huang, K., Peng, Y., Gao, Y., Shi, J., Li, H., Mo, X., Huang, H., Gao, Y., Ding, L., and Yang, J. (2019). High-Performance Flexible Perovskite Solar Cells via Precise Control of Electron Transport Layer. Adv. Energy Mater. *9*, 1901419. https://doi.org/10.1002/aenm.201901419.

8. Zhang, Y., Wu, Z., Li, P., Ono, L.K., Qi, Y., Zhou, J., Shen, H., Surya, C., and Zheng, Z. (2018). Fully solution-processed TCO-free semitransparent perovskite solar cells for tandem and flexible applications. Adv. Energy Mater. *8*, 1701569. https://doi.org/10.1002/aenm.201701569.

9. Werner, J., Boyd, C.C., Moot, T., Wolf, E.J., France, R.M., Johnson, S.A., van Hest, M.F.A.M., Luther, J.M., Zhu, K., Berry, J.J., and McGehee, M.D. (2020). Learning from existing photovoltaic technologies to identify alternative perovskite module designs. Energy Environ. Sci. *13*, 3393–3403. https://doi.org/10.1039/d0ee01923b.

10. Miasolé. https://miasole.com/new-world-record-efficiency-with-flexible-cigs-solar-cell/ (accessed 23th June 2023).

11. Feleki, B., Bouwer, R., Chandrashekar, S., Wienk, M.M., and Janssen, R.A.J. (2018). Perovskite Solar Cells on Steel Substrates: Optimization of a Dielectric/metal/dielectric Transparent Top Electrode. https://www.nanoge.org/proceedings/HOPV18/5abcda0ac4cdc7143337f160.

12. Kumar, S., Chouhan, A.S., Agarwal, H., and Avasthi, S. (2019). Perovskite Solar Cell Devices on Flexible Stainless-Steel Substrate (IEEE)), pp. 0477–0479.

13. Feleki, B.T., Bouwer, R.K.M., Wienk, M.M., and Janssen, R.A.J. (2022). Perovskite Solar Cells on Polymer-Coated Smooth and Rough Steel Substrates. Solar RRL *6*, 2100898. https://doi.org/10.1002/solr.202100898.

14. Feleki, B.T., Bouwer, R.K.M., Zardetto, V., Wienk, M.M., and Janssen, R.A.J. (2022). p-i-n Perovskite Solar Cells on Steel Substrates. ACS Appl. Energy Mater. *5*, 6709–6715. https://doi.org/10.1021/acsaem.2c00291.

15. Liu, C.M., Liu, W.L., Chen, W.J., Hsieh, S.H., Tsai, T.K., and Yang, L.C. (2005). ITO as a diffusion barrier between Si and Cu. J. Electrochem. Soc. *152*, G234. https://doi.org/10.1149/1.1860511.

16. Kim, Y., Lee, H.S., Yoon, G., and Park, S.H. (2020). Development of Indium-Tin Oxide Diffusion Barrier for Attaining High Reliability of Skutterudite Modules. ACS Energy Lett. *3*, 2989–2995. https://doi.org/10.1021/acsaem.0c00100.

17. Ben Haj Othmen, W., Ben Hamed, Z., Sieber, B., Addad, A., Elhouichet, H., and Boukherroub, R. (2018). Structural and optical characterization of p-type highly Fe-doped SnO$_2$ thin films and tunneling transport on SnO2:Fe/p-Si heterojunction. Appl. Surf. Sci. *434*, 879–890. https://doi.org/10.1016/j.apsusc.2017.11.019.

18. Poindexter, J.R., Hoye, R.L.Z., Nienhaus, L., Kurchin, R.C., Morishige, A.E., Looney, E.E., Osherov, A., Correa-Baena, J.P., Lai, B., Bulović, V., et al. (2017). High Tolerance to Iron Contamination in Lead Halide Perovskite Solar Cells. ACS Nano *11*, 7101–7109. https://doi.org/10.1021/acsnano.7b02734.

19. Duong, T., Pham, H., Yin, Y., Peng, J., Mahmud, M.A., Wu, Y., Shen, H., Zheng, J., Tran-Phu, T., Lu, T., et al. (2021). Efficient and stable wide bandgap perovskite solar cells through surface passivation with long alkyl chain organic cations. J. Mater. Chem. *9*, 18454–18465. https://doi.org/10.1039/d1ta05699a.

20. Zheng, J., Lau, C.F.J., Mehrvarz, H., Ma, F.-J., Jiang, Y., Deng, X., Soeriyadi, A., Kim, J., Zhang, M., Hu, L., et al. (2018). Large area efficient interface layer free monolithic perovskite/homo-junction-silicon tandem solar cell with over 20% efficiency. Energy Environ. Sci. *11*, 2432–2443. https://doi.org/10.1039/C8EE00689J.

21. Zheng, J., Duan, W., Guo, Y., Zhao, Z.C., Yi, H., Ma, F.J., Granados Caro, L., Yi, C., Bing, J., Tang, S., et al. (2023). Efficient Monolithic Perovskite-Si Tandem Solar Cell Enabled by an Ultra-Thin Indium Tin Oxide Interlayer. Energy Environ. Sci. *16*, 1223–1233. https://doi.org/10.1039/d2ee04007g.

22. Zheng, J., Hu, L., Yun, J.S., Zhang, M., Lau, C.-F.J., Bing, J., Deng, X., Ma, Q., Cho, Y., Fu, W., et al. (2018). Solution-Processed, Silver-Doped NiOx as Hole Transporting Layer for High Efficiency Inverted Perovskite Solar Cells. ACS Appl. Energy Mater. *1*, 561–570. https://doi.org/10.1021/acsaem.7b00129.

23. Aydin, E., Liu, J., Ugur, E., Azmi, R., Harrison, G.T., Hou, Y., Chen, B., Zhumagali, S.,

De Bastiani, M., Wang, M., et al. (2021). Ligand-bridged charge extraction and enhanced quantum efficiency enable efficient n–i–p perovskite/silicon tandem solar cells. Energy Environ. Sci. 14, 4377–4390. https://doi.org/10.1039/d1ee01206a.

24. Ho-Baillie, A.W.Y., Zheng, J., Mahmud, M.A., Ma, F.-J., McKenzie, D.R., and Green, M.A. (2021). Recent progress and future prospects of perovskite tandem solar cells. Appl. Phys. Rev. 8, 041307. https://doi.org/10.1063/5.0061483.

25. Xie, J., Yu, X., Sun, X., Huang, J., Zhang, Y., Lei, M., Huang, K., Xu, D., Tang, Z., Cui, C., and Yang, D. (2016). Improved performance and air stability of planar perovskite solar cells via interfacial engineering using a fullerene amine interlayer. Nano Energy 28, 330–337. https://doi.org/10.1016/j.nanoen.2016.08.048.

26. Cho, Y., Ohkita, H., Li, Y., Bing, J., Zheng, J., Huang, S., and Ho-Baillie, A. (2019). The Effect of 4-tert-Butylpyridine Removal on Efficiency and Thermal Stability in Perovskite Solar Cells. J. Photopolym. Sci. Technol. 32, 715–720. https://doi.org/10.2494/photopolymer.32.715.

27. Jeong, S.Y., Kim, H.S., and Park, N.G. (2022). Challenges for Thermally Stable Spiro-MeOTAD toward the Market Entry of Highly Efficient Perovskite Solar Cells. ACS Appl. Mater. Interfaces 14, 34220–34227. https://doi.org/10.1021/acsami.1c21852.

28. Tang, S., Peracchi, S., Pastuovic, Z., Liao, C., Xu, A., Bing, J., Zheng, J., Mahmud, M.A., Wang, G., Townsend-Medlock, E.D., et al. (2023). Effect of Hole Transport Materials and Their Dopants on the Stability and Recoverability of Perovskite Solar Cells on Very Thin Substrates after 7 MeV Proton Irradiation. Adv. Energy Mater. 13, 2300506. https://doi.org/10.1002/aenm.202300506.

29. Kim, J., Park, N., Yun, J.S., Huang, S., Green, M.A., and Ho-Baillie, A.W. (2017). An effective method of predicting perovskite solar cell lifetime–Case study on planar $CH_3NH_3PbI_3$ and $HC(NH_2)_2PbI_3$ perovskite solar cells and hole transfer materials of spiro-OMeTAD and PTAA. Sol. Energy Mater. Sol. Cells 162, 41–46. https://doi.org/10.1016/j.solmat.2016.12.043.

30. Gallardo, J., Galliano, P., and Durán, A. (2001). Bioactive and protective sol-gel coatings on metals for orthopaedic prostheses. J. Sol. Gel Sci. Technol. 21, 65–74. https://doi.org/10.1023/A:1011257516468.

31. Chaurasia, S., Raghavan, S., and Avasthi, S. (2017). Laser Crystallization of Amorphous Germanium on Titanium Nitride-Coated Steel for Low-Cost GaAs Solar-Cells (IEEE)), pp. 837–840.

32. Sun, K., Liu, F., Huang, J., Yan, C., Song, N., Sun, H., Xue, C., Zhang, Y., Pu, A., Shen, Y., et al. (2018). Flexible kesterite Cu_2ZnSnS_4 solar cells with sodium-doped molybdenum back contacts on stainless steel substrates. Sol. Energy Mater. Sol. Cells 182, 14–20. https://doi.org/10.1016/j.solmat.2018.02.036.

33. Giannuzzi, L.A., and Stevie, F.A. (1999). A review of focused ion beam milling techniques for TEM specimen preparation. Micron 30, 197–204. https://doi.org/10.1016/S0968-4328(99)00005-0.

34. Sentaurus, T. Technology Computer Aided Design (TCAD). Synopsys, Zürich, Switzerland.